To cite this version :

Rachele ALLENA - Mechanical modelling of confined cell migration across constricted-curved micro-channels - Molecular and Cellular Biomechanics - Vol. 11, n°3, p.185-208 - 2014

Mechanical Modelling of Confined Cell Migration Across Constricted-curved Micro-channels

R. Allena[*],[†]

Abstract: Confined migration is a crucial phenomenon during embryogenesis, immune response and cancer. Here, a two-dimensional finite element model of a HeLa cell migrating across constricted–curved micro-channels is proposed. The cell is modelled as a continuum with embedded cytoplasm and nucleus, which are described by standard Maxwell viscoelastic models. The decomposition of the deformation gradient is employed to define the cyclic active strains of protrusion and contraction, which are synchronized with the adhesion forces between the cell and the substrate. The micro-channels are represented by two rigid walls and exert an additional viscous force on the cell boundaries. Five configurations have been tested: 1) top constriction, 2) top-bottom constriction, 3) shifted top-bottom constriction, 4) embedded obstacle and 5) bending micro-channel. Additionally, for the first four micro-channels both sub-cellular and sub-nuclear constrictions have been obtained, while for the fifth micro-channel three types of bending have been investigated (‘curved’, ‘sharp’ and ‘sharper’). For each configuration, several parameters such as the cell behaviour, the covered distance, the migration velocity, the ratio between the cell and the nucleus area as well as the cell-substrate and cell-channel surfaces forces have been evaluated. The results show once more the fundamental role played by mechanics of both the cell and the environment.

Keywords: Confined cell migration, Curved micro-channel, Continuum mechanics, Computational mechanics.

1 Introduction

Cell migration in confinement is proper to several biological phenomena such as embryogenesis, immune response and cancer [1, 2]. Although cell migration on two-dimensional (2D) flat substrates has been largely investigated during the last few years, the mechanical principles triggering migration of cells in three-

---

[*] Arts et Metiers ParisTech, LBM, 151 Bd de l’hôpital, 75013 Paris, France.

[†] Corresponding author. E-mail: rachele.allena@ensam.eu

dimensional (3D) confined environments such as fibres networks are still little known. In fact, in addition to the external stimuli such as attractant molecules, the geometry and the mechanical nature of the extracellular matrix (ECM) may play a critical role during *in vivo* migration [3–5]. It has been shown that the width of the ECM pores, the ECM alignment and stiffness as well as the fibres density are fundamental parameters triggering or inhibiting the cell movement [2–9]. Therefore, in order to efficiently move within the fibres network, the cell has to constantly adapt its shape and its migratory behaviour.

Several experimental and numerical studies can be found in the literature, which focus on specific aspects of confined migration.

The former employ:

- gels or lattices [9] allowing to acquire very simplified systems for which, however, many physical parameters (i.e. gel density and elasticity or local constrictions) affecting the global cell motility are difficult to handle [9–11];
- micro-structures obtained through micro-laser techniques [12] or photolithography [13] for which the geometrical characteristics may be varied and tuned. Such techniques have been used to reproduce cell migration under confinement for cancer [14, 15] and immune [16] cells or neurons [17].

The latter propose Cellular Potts [18, 19], hybrid agent based finite element [20], energetic continuum [21], multi-physics [22] or purely mechanical [23] models which aim to evaluate the cell internal organization, the role of the nucleus and the migration strategy adopted by the cell according to the environment. More recently, Scianna and Preziosi [24] have presented an extension of their previous model in which migration takes place across two perpendicular micro-channels equal in width and length. In these works, the ECM is considered and represented as a regular geometry (i.e. tracks or micro-channels). Nevertheless, the ECM may be composed by fibres, which can be randomly aligned or form gaps of variable dimensions and radius of curvature leading to more complex geometries and forcing the cell to take turns and squeeze.

Here, the objective of the present work is to improve the previous model proposed in [23] in order to evaluate cell migration across micro-channels presenting simultaneously a parameterized curved shape and a constriction. The cell is modelled as a continuum with embedded cytoplasm and nucleus, which are defined by specific characteristic functions and considered as viscoelastic. The cell motility is determined by the synchronization between the active strains (i.e. protrusion and contraction), which are described through the decomposition of the deformation gradient, and the viscous adhesion forces between the cell and the substrate. The constricted-curved micro-channels are represented by two rigid walls, each defined by a characteristic function, and exert an additional viscous normal force on the cell boundaries. The geometrical parameters of the micro-channels have been tuned *ad hoc* and five configurations have been obtained.

In the next sections the geometry of the micro-channels (Sec. 2.1) and of the cell (Sec. 2.2) are presented as well as the cell constitutive law (Sec. 2.2) and the mechanical approach used to describe both the adhesion forces (Sec. 2.2) and the active strains (Sec. 2.3). In Sec. 3.1 and 3.2, the results are discussed by evaluating several parameters such as the cell behaviour during migration, the migration velocity and the cell-substrate and cell-channel surface forces. Finally, a comparison with previous models from the same author is proposed in Sec. 3.3.

2 The model

2.1 Micro-channels

We consider five different micro-channels $\Omega_{channel,i}$ (the subscript 'i'indicates the micro-channel number), each one represented by a upper (Ω_{uw}) and a lower (Ω_{lw}) rigid walls, which are spatially arranged as follows:

1) top constriction micro-channel or $\Omega_{channel,1}$: the lower wall is straight, while the upper wall is inward convex (Fig. 1a);

2) top-bottom constriction micro-channel or $\Omega_{channel,2}$: the lower and the upper walls are inward convex (Fig. 1b);

3) shifted top-bottom constriction micro-channel or $\Omega_{channel,3}$: the lower and the upper walls are inward convex and additionally shifted along the $x-$axis (Fig. 1c);

4) embedded obstacle micro-channel or $\Omega_{channel,4}$: the lower and the upper walls are both outward convex and a circular obstacle is placed at the centre of the micro-channel (Fig. 1d);

5) bending micro-channel or $\Omega_{channel,5}$: the lower and the upper walls are outward and inward convex, respectively (Fig. 2a).

For each geometry, two characteristic functions are employed to describe respectively Ω_{uw} and Ω_{lw} as follows

$$
\begin{aligned}
h_{uw,i}(\boldsymbol{p}) &= \begin{cases} 1 & \text{if } \; l_{uw,i} < 1 \\ 0 & \text{otherwise} \end{cases} \\
h_{lw,i}(\boldsymbol{p}) &= \begin{cases} 1 & \text{if } \; l_{lw,i} < 1 \\ 0 & \text{otherwise} \end{cases}
\end{aligned}
\qquad (1)
$$

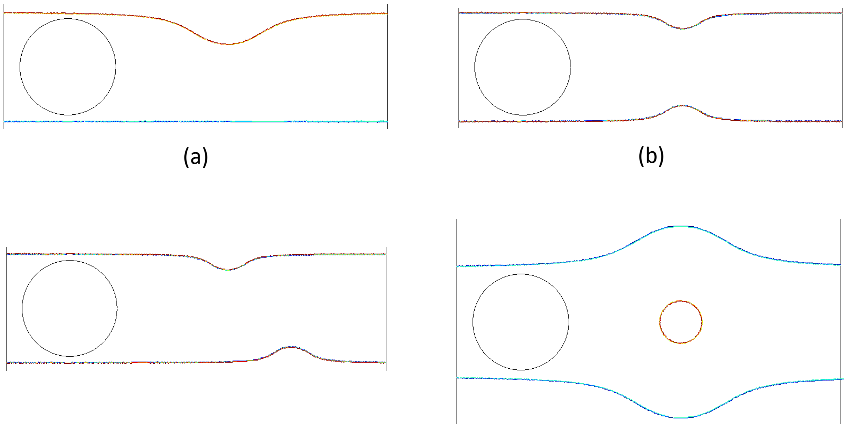

(a) (b) (c) (d)

Figure 1: Geometries of the micro-channels: (a) top constriction ($\Omega_{channel,1}$), (b) top-bottom constriction ($\Omega_{channel,3}$), (c) shifted top-bottom constriction ($\Omega_{channel,3}$) and (d) embedded obstacle micro-channel ($\Omega_{channel,4}$).

where $l_{uw,i}$ and $l_{lw,i}$ are two level set functions expressed as

$$
\begin{aligned}
l_{uw,1} &= -\left(y-y_{0,1}\right)\left[\left(x-x_{0u,1}\right)^2+\left(y-y_{0,1}\right)^2+\left(y+y_{0,1}\right)\right]\\
l_{uw,2} = l_{uw,3} &= -\left(y-y_{0,i}\right)\left[\left(x-x_{0u,i}\right)^2+\left(y-y_{0,i}\right)^2-r_{uw,i}^3\right]\\
l_{uw,4} &= \left(y-y_{0,4}\right)\left[\left(x-x_{0u,4}\right)^2+\left(y-y_{0,4}\right)^2-r_{uw,4}^3\right]\\
l_{uw,5} &= -\left(y-y_{0,5}\right)\left[\left(x-x_{0u,5}\right)^j+\left(y-y_{0,5}\right)^j-r_{uw,5}^k\right]
\end{aligned}
\tag{2}
$$

$$
\begin{aligned}
l_{lw,1} = l_{lw,4} &= -\left(y+y_{0,i}\right)\left[\left(x-x_{0l,i}\right)^2+\left(y+y_{0,i}\right)^2-r_{lw,i}^3\right]\\
l_{lw,2} = l_{lw,3} &= \left(y+y_{0,i}\right)\left[\left(x-x_{0l,i}\right)^2+\left(y+y_{0,i}\right)^2-r_{lw,i}^3\right]\\
l_{lw,5} &= -\left(y+y_{0,5}\right)\left[\left(x-x_{0l,5}\right)^j+\left(y+y_{0,5}\right)^j-r_{lw,5}^k\right]
\end{aligned}
\tag{3}
$$

Thus, the micro-channel $\Omega_{channel,i}$ is the sum of the two previous characteristic functions as follows

$$\Omega_{channel,i} = h_{uw,i}\left(\boldsymbol{p}\right)+h_{lw,i}\left(\boldsymbol{p}\right) \tag{4}$$

Additionally, for $\Omega_{channel,4}$ Eq. (4) is slightly modified and reads

$$\Omega_{channel,4} = h_{uw,4}\left(\boldsymbol{p}\right)+h_{lw,4}\left(\boldsymbol{p}\right)+h_{obstacle}\left(\boldsymbol{p}\right) \tag{5}$$

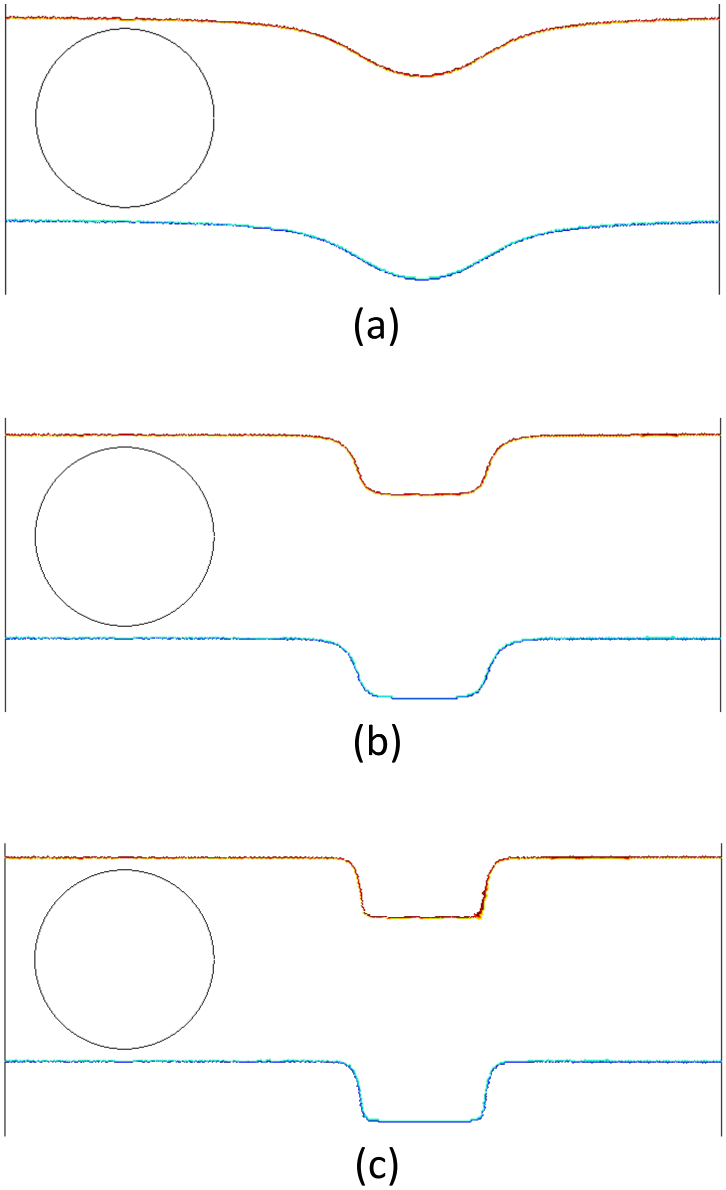

Figure 2: Geometries of $\Omega_{channel,5}$: (a) ‘curved’, (b) ‘sharp’ and (c) ‘sharper’ bending.

where $h_{obstacle}(\boldsymbol{p})$ is the characteristic function of the central circular obstacle $\Omega_{obstacle}$ expressed as

$$h_{obstacle}(\boldsymbol{p}) = \begin{cases} 1 & \text{if} \quad l_{obstacle} < 1 \\ 0 & \text{otherwise} \end{cases} \tag{6}$$

with $l_{obstacle} = (x - x_{0,4})^2 + y^2 - r_4^2$ and r_4 the radius of the circle.

When the cell enters into the micro-channel, it is then submitted to a viscous force $\boldsymbol{f}_{channel}$, which is the sum of an upper ($\boldsymbol{f}_{uw_i}$) and a lower ($\boldsymbol{f}_{lw_i}$) force that read

$$\begin{aligned} \boldsymbol{f}_{uw_i}(\boldsymbol{n}_{uw,i}) &= -\mu_{channel} \frac{1}{(l_{uw,i}+1)^8 + \alpha} \left(\frac{\partial \boldsymbol{u}}{\partial t}, \boldsymbol{n}_{uw,i} \right) \boldsymbol{n}_{uw,i} \quad \text{on} \quad \partial\Omega_{uw,i} \\ \boldsymbol{f}_{lw_i}(\boldsymbol{n}_{lw,i}) &= -\mu_{channel} \frac{1}{(l_{lw,i}+1)^8 + \alpha} \left(\frac{\partial \boldsymbol{u}}{\partial t}, \boldsymbol{n}_{lw,i} \right) \boldsymbol{n}_{lw,i} \quad \text{on} \quad \partial\Omega_{lw,i} \end{aligned} \tag{7}$$

where $\mu_{channel}$ is the viscosity of the micro-channel, α is a constant and $(\boldsymbol{a}, \boldsymbol{b})$ defines the scalar product between two vectors $\boldsymbol{a}$ and $\boldsymbol{b}$. The outward normal vectors $\boldsymbol{n}_{uw,i}$ and $\boldsymbol{n}_{lw,i}$ to the boundaries $\partial\Omega_{uw,i}$ and $\partial\Omega_{lw,i}$ of the upper and lower wall are given by

$$\begin{aligned} \boldsymbol{n}_{uw,i} &= h'(l_{uw,i}) \frac{\nabla l_{uw,i}}{\|\nabla l_{uw,i}\|} \\ \boldsymbol{n}_{lw,i} &= h'(l_{lw,i}) \frac{\nabla l_{lw,i}}{\|\nabla l_{lw,i}\|} \end{aligned} \tag{8}$$

where h' indicates the Dirac delta function.

Finally, for $\Omega_{channel,4}$ an additional force $f_{obstacle}(n_{obstacle})$ is exerted along the external boundary of the obstacle and reads

$$\begin{aligned} \boldsymbol{f}_{obstacle}(\boldsymbol{n}_{obstacle}) = &- \mu_{channel} \frac{1}{(l_{obstacle}+1)^8 + \alpha} \left(\frac{\partial \boldsymbol{u}}{\partial t}, \boldsymbol{n}_{obstacle} \right) \boldsymbol{n}_{obstacle} \\ &\text{on} \quad \partial\Omega_{obstacle} \end{aligned} \tag{9}$$

with $\boldsymbol{n}_{obstacle} = h'(l_{obstacle}) \frac{\nabla l_{obstacle}}{\|\nabla l_{obstacle}\|}$.

2.2 Cell geometry and mechanics

At the initial time point, the cell Ω_{cell} is represented by a circle of radius r_{cell} and includes the cytoplasm ($\Omega_{cytoplasm}$) and the nucleus ($\Omega_{nucleus}$) (Fig. 3a), which are assumed to be viscoelastic and modelled by two standard Maxwell models [23, 25, 26]. The nucleus is composed by the nuclear lamina (Ω_{lamina}) and the nucleoplasm

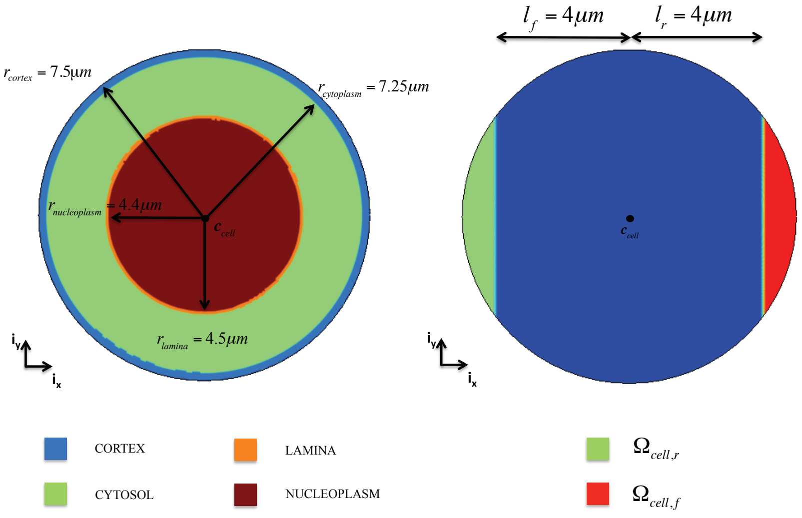

(a) (b)

Figure 3: Geometry of the cell (a) and frontal and rear adhesion surfaces (b).

($\Omega_{nucleoplasm}$), while the cytoplasm is constituted by the cell cortex (Ω_{cortex}) and the cytosol ($\Omega_{cytosol}$). Each component is described through a characteristic function as follows

$$h_{cortex}(\boldsymbol{p}) = \begin{cases} 1 & \text{if } \; r^2_{cytoplasm} < \|\boldsymbol{p} - \boldsymbol{c}_{cell}\| < r^2_{cortex} \\ 0 & \text{otherwise} \end{cases} \tag{10}$$

$$h_{cytosol}(\boldsymbol{p}) = \begin{cases} 1 & \text{if } \; r^2_{lamina} < \|\boldsymbol{p} - \boldsymbol{c}_{cell}\| < r^2_{cytosol} \\ 0 & \text{otherwise} \end{cases} \tag{11}$$

$$h_{lamina}(\boldsymbol{p}) = \begin{cases} 1 & \text{if } \; r^2_{nucleoplasm} < \|\boldsymbol{p} - \boldsymbol{c}_{cell}\| < r^2_{lamina} \\ 0 & \text{otherwise} \end{cases} \tag{12}$$

$$h_{nucleoplasm}(\boldsymbol{p}) = \begin{cases} 1 & \text{if } \; \|\boldsymbol{p} - \boldsymbol{c}_{cell}\| < r^2_{nucleoplasm} \\ 0 & \text{otherwise} \end{cases} \tag{13}$$

where $\boldsymbol{p} = \boldsymbol{x} - \boldsymbol{u}$, with $\boldsymbol{x}$ and $\boldsymbol{u}$ being respectively the actual position and the displacement, $\boldsymbol{c}_{cell}$ is the cell centre and r_{cortex}, $r_{cytosol}$, r_{lamina} and $r_{nucleoplasm}$ are the external radius of the cell cortex, the cytosol, the nuclear lamina and nucleoplasm respectively (Fig. 3a). Then, the cytoplasm $\Omega_{cytoplasm}$ and the nucleus $\Omega_{nucleus}$ domains are defined by the following characteristic functions

$$\begin{aligned} h_{cytoplasm}(\boldsymbol{p}) &= h_{cortex}(\boldsymbol{p}) + h_{cytosol}(\boldsymbol{p}) \\ h_{nucleus}(\boldsymbol{p}) &= h_{lamina}(\boldsymbol{p}) + h_{nucleoplasm}(\boldsymbol{p}) \end{aligned} \tag{14}$$

The global equilibrium of the system can be expressed as

$$\rho \boldsymbol{a} = \boldsymbol{Div}_p \left(J \boldsymbol{\sigma} \boldsymbol{F}^{-T} \right) + \boldsymbol{f}_{adh} + \boldsymbol{f}_{channel} \tag{15}$$

with ρ the global cell density, $\boldsymbol{a}$ the acceleration, $\boldsymbol{Div}_p$ the divergence with respect to the initial position $\boldsymbol{p}$, J the determinant of the deformation gradient $\boldsymbol{F}$ and $\boldsymbol{F}^{-T}$ the inverse transpose of the matrix $\boldsymbol{F}$ [26, 27]. $\boldsymbol{f}_{adh}$ defines the viscous adhesion forces [28–31] between the cell and the substrate which are cyclically activated at the front ($\Omega_{cell,f}$) and at the back ($\Omega_{cell,r}$) of the cell (Fig. 3b), which are expressed as

$$\begin{aligned} h_{cell,f}(\boldsymbol{p}) &= \begin{cases} 1 & (\boldsymbol{p} - \boldsymbol{c}_{cell}, \boldsymbol{i}_x) > l_f \\ 0 & \text{otherwise} \end{cases} \\ h_{cell,r}(\boldsymbol{p}) &= \begin{cases} 1 & (\boldsymbol{p} - \boldsymbol{c}_{cell}, \boldsymbol{i}_x) < -l_r \\ 0 & \text{otherwise} \end{cases} \end{aligned} \tag{16}$$

with l_f and l_r the distances of $\boldsymbol{c}_{cell}$ from the boundaries $\partial\Omega_{cell,f}$ and $\partial\Omega_{cell,r}$ respectively (Fig. 3b).

Thus, $\boldsymbol{f}_{adh}$ is the composition of a frontal ($\boldsymbol{f}_{adh,f}$) and a rear ($\boldsymbol{f}_{adh,r}$) component that read

$$\begin{aligned} \boldsymbol{f}_{adh,f}(\boldsymbol{n}_{cell}) &= -\mu_{adh} h_{sync} \left(-\frac{\partial \boldsymbol{F}_{cytosol,a}}{\partial t} \right) \boldsymbol{v} \quad \text{on} \quad \Omega_{cell,f} \\ \boldsymbol{f}_{adh,r}(\boldsymbol{n}_{cell}) &= -\mu_{adh} h_{sync} \left(\frac{\partial \boldsymbol{F}_{cytosol,a}}{\partial t} \right) \boldsymbol{v} \quad \text{on} \quad \Omega_{cell,r} \end{aligned} \tag{17}$$

with $\boldsymbol{n}_{cell}$ the outward normal to the cell boundary, μ_{adh} the friction coefficient, $\boldsymbol{v}$ the velocity and $\boldsymbol{F}_{cytosol,a}$ the solid active deformation tensor defined in the next section (Sec. 2.3). The characteristic function $h_{sync}\left(\mp \frac{\partial \boldsymbol{F}_{cytosol,a}}{\partial t}\right)$ couples the adhesion forces with the active strains of protrusion and contraction [30, 31], which are described in the next section.

2.3 Active strains

During migration, we observe two main phases: i) the protrusion and the adhesion at the rear edge and ii) the contraction and the adhesion at the frontal edge [30]. Here, it is assumed that such an oscillatory movement of the cell is triggered by the periodic polymerization and depolymerization of the actin filaments [32], which are embedded in the cytosol. The former only occurs at the front of the cell, while the latter takes place from the front towards the rear of the cell. Therefore, although not submitted to any active strain, the nucleus interacts with the surrounding cytosol apart from the protrusion phase [33]. Additionally, an external attractive source is introduced at 0° at the right side of the micro-channel, so that the direction of migration is imposed and corresponds to the horizontal axis $\boldsymbol{i}_x$.

The solid active deformation tensor $\boldsymbol{F}_{cytosol,a}$ [23] reads

$$\boldsymbol{F}_{cytosol,a} = \begin{cases} e_{a0} \sin\left(2\pi \frac{t}{T}\right) h_{cytosol,f} \boldsymbol{i}_x \otimes \boldsymbol{i}_x & \text{if} \quad \sin\left(2\pi \frac{t}{T}\right) > 0 \\ \frac{e_{a0}}{2} \sin\left(2\pi \frac{t}{T}\right) h_{cytosol} \boldsymbol{i}_x \otimes \boldsymbol{i}_x & \text{if} \quad \sin\left(2\pi \frac{t}{T}\right) < 0 \end{cases} \tag{18}$$

where e_{a0} is the amplitude of the active strain, t is time, T is the migration period and $\otimes$ indicates the tensorial product. $h_{cytosol,f}$ is a characteristic function describing the portion of cytosol where the polymerization of the actin filaments takes place and reads

$$h_{cytosol,f}(\boldsymbol{p}) = \begin{cases} h_{cytosol} & \text{if} \quad \boldsymbol{p} > \boldsymbol{c}_{cell} \\ 0 & \text{otherwise} \end{cases} \tag{19}$$

3 Results

COMSOL Multiphysics® 3.5a has been used to run all the simulations. As in [23], the model represents a HeLa cell. The characteristic functions presented in Sec. 2.2 have been used to implicitly describe the cytoplasm and the nucleus components in order to be able to define the parameters of the standard Maxwell models [23]. The radius r_{cortex}, $r_{cytosol}$,r_{lamina} and $r_{nucleoplasm}$ of the cell have been chosen equal to 7.5 μm [34, 35], 7.25 μm, 4.5 μm and 4.4 μm respectively, which leads to a cell cortex (t_{cortex}) and a nuclear lamina (t_{lamina}) thicknesses equal to 0.25 μm [36–38] and 0.1 μm [39] respectively. The nominal values of the Young moduli $E_{cortex,0}$ of the cell cortex and $E_{cytosol,0}$ of the cytosol have been chosen equal to 100 Pa and 10 Pa [40], respectively. For the nucleus, assuming that its stiffness is mostly provided by the nuclear lamina, $E_{lamina,0}$ and $E_{nucleoplasm,0}$ have been set to 3000 Pa [41, 42] and 25 Pa [43], respectively. Such moduli have been recalculated according to a simple spatial homogenization approach [25, 44] and to the surface occupied by each component in the cell to obtain E_{cortex},$E_{cytosol}$,E_{lamina} and$E_{nucleoplasm}$. The Poisson's ratios ν_{cortex} and ν_{lamina} have been set to 0.3, while $\nu_{cytosol}$ and $\nu_{nucleoplasm}$ to 0.4. The viscosities $\mu_{cytosol}$ and $\mu_{nucleoplasm}$ are equal to 3×10^5Pa-s [45, 46]. The global cell density ρ has been set to 1000 kg/m^3 [47] and the viscous friction coefficient μ_{adh} is equal 10^8Pa-s/m. Finally, the intensity of the active strain e_{a0} and the migration period T have been chosen equal to 0.2 and 600 s respectively.

The geometrical and mechanical parameters of the cell have been reported in Table 1.

Table 1: Main geometrical and material parameters of the model.

Parameter	**Description**	**Value**	**Unit**	**Reference**
r_{cell}	Cell radius	7.5	μm	[34, 35]
r_{cortex}	Cortex radius	7.5	μm	
$r_{cytosol}$	Cytosol radius	7.25	μm	
r_{lamina}	Lamina radius	4.5	μm	
$r_{nucleoplasm}$	Nucleoplasm radius	4.4	μm	
t_{cortex}	Cortex thickness	0.25	μm	[36–38]
t_{lamina}	Lamina thickness	0.1	μm	[39]
l_f	Distance cell centre – boundary of frontal adhesion region	4	μm	
l_r	Distance cell centre – boundary of rear adhesion region	4	μm	
Ω_{cell}	Initial cell area	176.6	μm^2	
Ω_{cortex}	Initial cortex area	11.6	μm^2	
$\Omega_{cytosol}$	Initial cytosol area	101.4	μm^2	
$\Omega_{cytoplasm}$	Initial cytoplasm area	113	μm^2	
Ω_{lamina}	Initial lamina area	2.8	μm^2	
$\Omega_{nucleoplasm}$	Initial nucleoplasm area	60.8	μm^2	
$\Omega_{nucleus}$	Initial nucleus area	63.6	μm^2	
Ω_f	Initial frontal adhesion region area	31	μm^2	
Ω_r	Initial rear adhesion region area	31	μm^2	
$E_{cortex,0}$	Nominal cortex Young modulus	100	Pa	
$E_{cytosol,0}$	Nominal cytosol Young modulus	10	Pa	[40]
$E_{lamina,0}$	Nominal lamina Young modulus	3000	Pa	[41, 42]
$E_{nucleoplasm,0}$	Nominal nucleoplasm Young modulus	25	Pa	[43]
E_{cortex}	Equivalent cortex Young modulus	15	Pa	
$E_{cytosol}$	Equivalent cytosol Young modulus	8	Pa	
E_{lamina}	Equivalent lamina Young modulus	196	Pa	
$E_{nucleoplasm}$	Equivalent nucleoplasm Young modulus	23	Pa	
ν_{cortex}	Cortex Poisson ratio	0.3		
$\nu_{cytosol}$	Cytosol Poisson ratio	0.4		
ν_{lamina}	Lamina Poisson ratio	0.3		
$\nu_{nucleoplasm}$	Nucleoplasm Poisson ratio	0.4		
$\mu_{cytosol}$	Cytosol viscosity	3×10^5	Pa-s	[45, 46]
$\mu_{nucleoplasm}$	Nucleoplasm viscosity	3×10^5	Pa-s	[45, 46]
ρ	Cell density	1000	kg/m^3	[47]
e_{a0}	Amplitude of the active strain	0.8		
T	Migration period	600	s	

3.1 Cell behaviour overview

Here, the results obtained for $\Omega_{channel,1}$to $\Omega_{channel,4}$ are presented. These micro-channels show a specific type of constriction (Sec. 2.1, Fig. 1a:d). Then, their geometrical parameters have been tuned (see Table 2) in order to obtain two series of simulations for which the constrictions are i) sub-cellular (12μm) and ii) sub-nuclear (7μm), respectively. For all the simulations, the total length and the viscous penalty coefficient ($\mu_{channel}$) of the micro-channels have been set to 40 μm and 10^{10} Pa-s/m, respectively. A time interval of 9000 s has been considered for micro-channels $\Omega_{channel,1}$ to $\Omega_{channel,3}$, while for $\Omega_{channel,4}$ a longer period (12000 s) has been tested. The cell behaviour has been investigated for each of the previous configurations and the main results are reported in Table 3.

The efficiency of the migration has been evaluated in terms of covered distance and migration velocity. For each micro-channel, whether the constriction is sub-cellular or sub-nuclear, the cell is permeative [15, 23, 24] since it is able to migrate through the micro-channel and reach the opposite side. In order to do so, the cell must squeeze or turn or both simultaneously (see Fig. 4,5). The covered distance goes from a minimal value of 43.8 μm (sub-nuclear $\Omega_{channel,2}$) to a maximal value of 48.2 μm (sub-cellular $\Omega_{channel,4}$). The average velocity of the cell centre of inertia is between $0.65 \cdot 10^{-2} \mu$m/s ($\Omega_{channel,1}$) and $1.05 \cdot 10^{-2} \mu$m/s ($\Omega_{channel,4}$). Some peak is observed, especially for the sub-nuclear constrictions, when the cell migrates through the micro-channel narrowing. For instance, for $\Omega_{channel,2}$ and $\Omega_{channel,4}$, the maximal values are equal to $2.6 \cdot 10^{-2} \mu$m/s and $3 \cdot 10^{-2} \mu$m/s, respectively. Nevertheless, such values are still of the same order of magnitude of those experimentally observed for HeLa cells [34, 35] and, as found in [23], the velocity during the contraction phase is slightly higher than during the contraction phase.

For each simulation, three parameters have been defined [23]:

- $t_{contact}$ corresponds to the first contact between the cell and the upper or the lower wall of the micro-channel (or the obstacle for $\Omega_{channel,4}$);
- t_{exit} corresponds to the loss of contact between the cell and both micro-channel walls (and the obstacle for $\Omega_{channel,4}$);
- T_{entry} is the elapsed time between $t_{contact}$ and t_{exit}.

T_{entry} has been determined only for sub-cellular constrictions of $\Omega_{channel,2}$ and $\Omega_{channel,3}$ (2950 s and 4600 s respectively). For the other configurations in fact, the cell would certainly need more time to reacquire its initial shape. As a general remark, $t_{contact}$ is higher for sub-cellular constrictions than for sub-nuclear. This is mostly due to the fact that, in order to obtain sub-nuclear constrictions (Eqs.

Table 2: Geometrical parameters for the five micro-channels.

<table>
<tr><th rowspan="2">Parameter</th><th rowspan="2">Description</th><th colspan="3">Value</th><th rowspan="2">Units</th></tr>
<tr><th>Sub-cellular</th><th colspan="2">Sub-nuclear</th></tr>
<tr><td>$x_{0u,1}$</td><td>x-axis upper wall coordinate $\Omega_{channel,1}$</td><td>25</td><td colspan="2">25</td><td>μm</td></tr>
<tr><td>$x_{0u,2}$</td><td>x-axis upper wall coordinate $\Omega_{channel,2}$</td><td>25</td><td colspan="2">25</td><td></td></tr>
<tr><td>$x_{0u,3}$</td><td>x-axis upper wall coordinate $\Omega_{channel,3}$</td><td>25</td><td colspan="2">25</td><td>μm</td></tr>
<tr><td>$x_{0u,4}$</td><td>x-axis upper wall coordinate $\Omega_{channel,4}$</td><td>25</td><td colspan="2">25</td><td>μm</td></tr>
<tr><td rowspan="2">$x_{0u,5}$</td><td rowspan="2">x-axis upper wall coordinate $\Omega_{channel,5}$</td><th>‘curved’</th><th>‘sharp’</th><th>‘sharper’</th><td rowspan="2">μm</td></tr>
<tr><td>25</td><td>25</td><td>25</td></tr>
<tr><td>x_{0l1}</td><td>x-axis lower wall coordinate $\Omega_{channel,1}$</td><td>25</td><td colspan="2">25</td><td>μm</td></tr>
<tr><td>$x_{0l,2}$</td><td>x-axis lower wall coordinate $\Omega_{channel,2}$</td><td>25</td><td colspan="2">25</td><td></td></tr>
<tr><td>$x_{0l,3}$</td><td>x-axis lower wall coordinate $\Omega_{channel,3}$</td><td>35</td><td colspan="2">35</td><td>μm</td></tr>
<tr><td>$x_{0l,4}$</td><td>x-axis lower wall coordinate $\Omega_{channel,4}$</td><td>25</td><td colspan="2">25</td><td>μm</td></tr>
<tr><td rowspan="2">$x_{0l,5}$</td><td rowspan="2">x-axis lower wall coordinate $\Omega_{channel,5}$</td><th>‘curved’</th><th>‘sharp’</th><th>‘sharper’</th><td rowspan="2">μm</td></tr>
<tr><td>25</td><td>25</td><td>25</td></tr>
<tr><td rowspan="2">$y_{0,1}$</td><td rowspan="2">y-axis coordinate $\Omega_{channel,1}$</td><td rowspan="2">8.5</td><th>Upper wall</th><th>Lower wall</th><td rowspan="2">μm</td></tr>
<tr><td>9.5</td><td>7.5</td></tr>
<tr><td>$y_{0,2}$</td><td>y-axis coordinate $\Omega_{channel,2}$</td><td>8.5</td><td colspan="2">8.5</td><td>μm</td></tr>
<tr><td>$y_{0,3}$</td><td>y-axis coordinate $\Omega_{channel,3}$</td><td>8.5</td><td colspan="2">8.5</td><td>μm</td></tr>
<tr><td>$y_{0,4}$</td><td>y-axis coordinate $\Omega_{channel,4}$</td><td>8.5</td><td colspan="2">8.5</td><td>μm</td></tr>
<tr><td rowspan="2">$y_{0,5}$</td><td rowspan="2">y-axis coordinate $\Omega_{channel,5}$</td><th>‘curved’</th><th>‘sharp’</th><th>‘sharper’</th><td rowspan="2">μm</td></tr>
<tr><td>8.5</td><td>8.5</td><td>8.5</td></tr>
<tr><td>$r_{uw,1}$</td><td>Radius upper wall $\Omega_{channel,1}$</td><td>5</td><td colspan="2">10</td><td>μm</td></tr>
<tr><td>$r_{uw,2}$</td><td>Radius upper wall $\Omega_{channel,2}$</td><td>2.5</td><td colspan="2">5</td><td>μm</td></tr>
<tr><td>$r_{uw,3}$</td><td>Radius upper wall$\Omega_{channel,3}$</td><td>2.5</td><td colspan="2">5</td><td>μm</td></tr>
<tr><td>$r_{uw,4}$</td><td>Radius upper wall$\Omega_{channel,4}$</td><td>6.5</td><td colspan="2">2.5</td><td>μm</td></tr>
<tr><td rowspan="2">$r_{uw,5}$</td><td rowspan="2">Radius upper wall$\Omega_{channel,5}$</td><th>‘curved’</th><th>‘sharp’</th><th>‘sharper’</th><td rowspan="2">μm</td></tr>
<tr><td>5</td><td>5</td><td>5</td></tr>
<tr><td>$r_{lw,2}$</td><td>Radius lower wall $\Omega_{channel,2}$</td><td>2.5</td><td colspan="2">5</td><td>μm</td></tr>
<tr><td>$r_{lw,3}$</td><td>Radius lower wall $\Omega_{channel,3}$</td><td>2.5</td><td colspan="2">5</td><td>μm</td></tr>
<tr><td>$r_{lw,4}$</td><td>Radius lower wall $\Omega_{channel,4}$</td><td>6.5</td><td colspan="2">2.5</td><td>μm</td></tr>
<tr><td rowspan="2">$r_{lw,5}$</td><td rowspan="2">Radius lower wall $\Omega_{channel,5}$</td><th>‘curved’</th><th>‘sharp’</th><th>‘sharper’</th><td rowspan="2">μm</td></tr>
<tr><td>5</td><td>5</td><td>5</td></tr>
<tr><td>r_4</td><td>Radius obstacle $\Omega_{obstacle}$</td><td>3</td><td colspan="2">4</td><td>μm</td></tr>
<tr><td rowspan="2">j</td><td rowspan="2">Power in Eq. [2] and [3]</td><th>‘curved’</th><th>‘sharp’</th><th>‘sharper’</th><td rowspan="2"></td></tr>
<tr><td>2</td><td>6</td><td>12</td></tr>
<tr><td rowspan="2">k</td><td rowspan="2">Power in Eq. [2] and [3]</td><th>‘curved’</th><th>‘sharp’</th><th>‘sharper’</th><td rowspan="2"></td></tr>
<tr><td>3</td><td>7</td><td>13</td></tr>
<tr><td>$\mu_{channel}$</td><td>Micro-channel viscosity</td><td>10^{10}</td><td colspan="2">10^{10}</td><td>Pa-s/m</td></tr>
<tr><td>α</td><td></td><td>0.1</td><td colspan="2"></td><td></td></tr>
</table>

Table 3: Main results for micro-channels $\Omega_{channel,1}$ to $\Omega_{channel,4}$.

	$\Omega_{channel,1}$		$\Omega_{channel,2}$		$\Omega_{channel,3}$		$\Omega_{channel,4}$	
	Sub-cellular	Sub-nuclear	Sub-cellular	Sub-nuclear	Sub-cellular	Sub-nuclear	Sub-cellular	Sub-nuclear
Migration behaviour	Permeative	Permeative	Permeative	Permeative	Permeative	Permeative	Permeative	Permeative
Covered distance (μm)	46.5	45.1	46.6	43.8	46.5	45.6	48.2	46.5
Average migration velocity (μm/s)	$0.65{\cdot}10^{-2}$ max $1.45{\cdot}10^{-2}$	$1.2{\cdot}10^{-2}$ max $1.98{\cdot}10^{-2}$	$0.75{\cdot}10^{-2}$ max $1.45{\cdot}10^{-2}$	$0.7{\cdot}10^{-2}$ max $2.6{\cdot}10^{-2}$	$0.75{\cdot}10^{-2}$ max $1.35{\cdot}10^{-2}$	$0.8{\cdot}10^{-2}$ max $1.7{\cdot}10^{-2}$	$0.8{\cdot}10^{-2}$ max $3{\cdot}10^{-2}$	$1.05{\cdot}10^{-2}$ max $3{\cdot}10^{-2}$
Entry time $t_{contact}$(s)	2450	550	3650	2400	3650	2400	3000	2450
Exit time t_{exit} (s)	-	-	6600	-	8250	-	-	-
Penetration period T_{entry}(s)	-	-	2950	-	4600	-	-	-
Maximal cell area/nucleus area (during T_{entry})	3.65	3.73	3.65	3.8	3.58	3.6	3.45	3.55
Minimal cell area/nucleus area (during T_{entry})	2.55	2.24	2.57	2.28	2.63	2.41	2.41	2.21
Maximal frontal cell-substrate surface force before $t_{contact}$ and after t_{exit} [Pa]	9.5	9.5	9.5	9.7	9.5	9.5	16.2	14.5
Maximal rear cell-substrate surface force before $t_{contact}$ and after t_{exit} [Pa]	2.8	0.4	2.8	4.8	2.8	3.8	5.5	7.3
Frontal cell-substrate surface force at $t_{contact}$ [Pa]	1.7	1	8	8	8	8	8	6
Rear cell-substrate surface force at $t_{contact}$ [Pa]	2.3	1.4	2.7	2.7	2.7	2.7	2.7	2.7
Cell-channel surface force at $t_{contact}$ [Pa]	1.5	2	1	1	1	1	1.8	1.1
Maximal cell-channel surface force during T_{entry} [Pa]	4	5.3	3.8	3.7	4.6	3	6	7.8

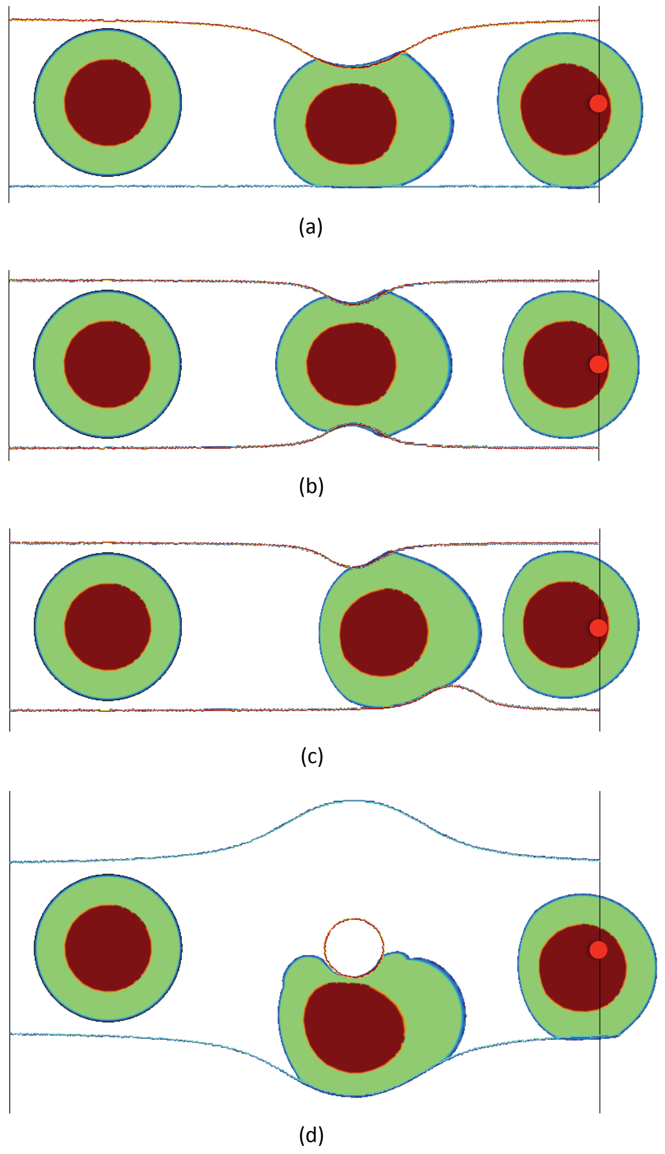

Figure 4: Migration through sub-cellular micro-channels at different time points. (a) Top constriction micro-channel (from left to right t = 0, 5000 s, 9000 s) (b) Top-bottom constriction micro-channel (from left to right t = 0, 5000 s, 9000 s) (c) Shifted top-bottom constriction micro-channel (from left to right t = 0, 5000 s, 9000 s) (d) Embedded obstacle micro-channel (from left to right t = 0, 7300 s, 12000 s) (blue= cell cortex, green = cytosol, orange = nuclear lamina, red = nucleoplasm, red circle = attractive source).

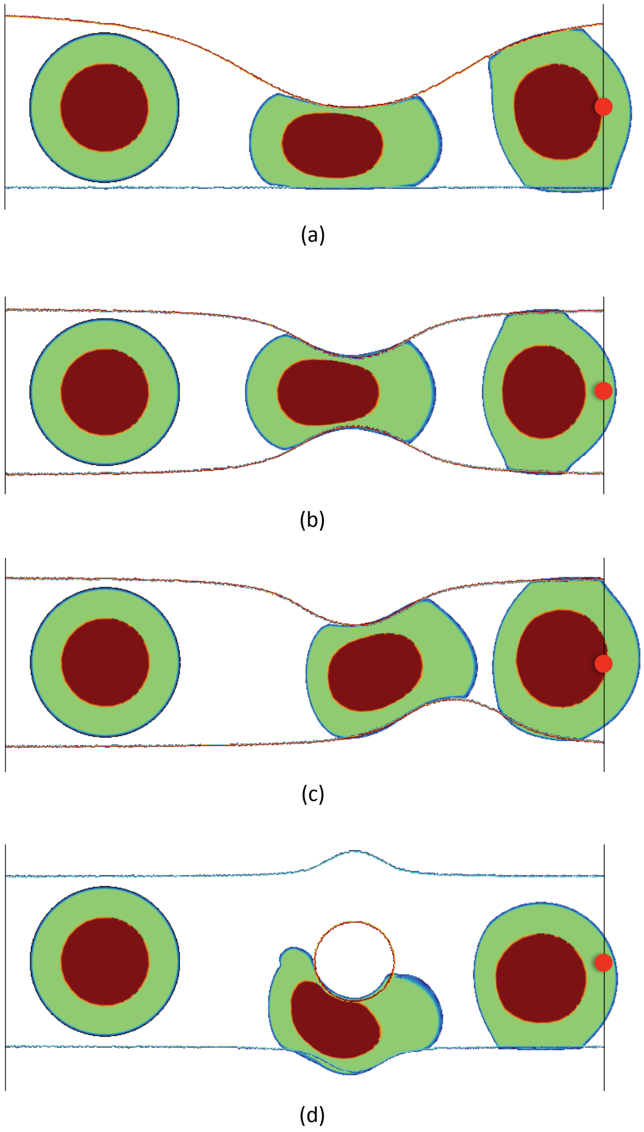

Figure 5: Migration through sub-nuclear micro-channels at different time points. (a) Top constriction micro-channel (from left to right t = 0, 5000 s, 9000 s) (b) Top-bottom constriction micro-channel (from left to right t = 0, 5000 s, 9000 s) (c) Shifted top-bottom constriction micro-channel (from left to right t = 0, 5000 s, 9000 s) (d) Embedded obstacle micro-channel (from left to right t = 0, 7300 s, 12000 s) (blue= cell cortex, green = cytosol, orange = nuclear lamina, red = nucleoplasm, red circle = attractive source).

(2) and (3)), the upper or the lower micro-channel walls (or both) start narrowing earlier (Fig. 1a:d), thus the cell come earlier into contact with the micro-channel.

The ratio between the total cell area and the nucleus area has also been evaluated. The initial value is equal to 2.8, but, due to the protrusion and contraction phases, it oscillates between a maximal value of 3.6 and 2.6 before before $t_{contact}$ and after t_{exit}, respectively. In Table 3, the values of the ratio during the penetration period T_{entry} have been reported. For the sub-cellular constrictions, no significant variations are observed. For the sub-nuclear constrictions instead, the ratio value decrease to 2.24, 2.28, 2.41 and 2.21 respectively for $\Omega_{channel,1}$, $\Omega_{channel,2}$, $\Omega_{channel,3}$ and $\Omega_{channel,4}$. For these configurations in fact, both the cytoplasm and the nucleus must squeeze in order for the cell to migrate through the narrowing region.

Finally, the cell-substrate and cell-channel forces have been evaluated. Due to the asymmetry of the active strain (Sec. 2.3) and according to Eq. [17] expressing the cell-substrate surface forces, a higher force was found at the frontal edge of the cell than at the rear. Specifically, the frontal cell-substrate force is comprised between 9.5 Pa and 16.2 Pa, while the rear cell-substrate force is comprised between 2.8 Pa and 7.3 Pa. As for the cell-channel surface force, it varies between a minimal value of 1 Pa at $t_{contact}$ and a maximal value of 7.8 Pa during the penetration period T_{entry}.

As mentioned above, the cell shows a permeative behaviour for all the configurations, either sub-cellular or sub-nuclear. In fact, the three conditions defined in [23] are respected here and more specifically:

- the cell-channel force is lower than the cell-substrate force at $t_{contact}$;
- the cell is able to penetrate the micro-channel thanks to a frontal edge protrusion whose length is larger than half the constriction width;
- during the penetration period T_{entry}, the cell-channel force is higher than the cell-substrate force so that the cell is maintained squeezed all time.

3.2 Bending channel

In this section the results for $\Omega_{channel,4}$ are discussed and reported in Table 4. Contrary to the previous ones, this micro-channel does not present any constriction, but the cell must turn in order to achieve the opposite side. By increasing the powers in Eqs. (2) and (3), the bending angle becomes closer to a right angle. Then, three configurations have been tested: i) 'curved' (Fig. 2a) ii) 'sharp' (Fig. 2b) and iii) 'sharper' (Fig. 2c) bending. In the three cases, the cell is permeative and progresses with an average velocity of the centre of inertia which is slightly higher (between $0.8{\cdot}10^{-2}\mu$m/s and $1.4{\cdot}10^{-2}\mu$m/s) than that found for the previous micro-channels (Sec. 3.1). Additionally, since the micro-channel induces the cell to turn but not to squeeze, the ratio between the total cell area and the nucleus area does not change significantly (maximal and minimal value during T_{entry} equal to 3.65 and 2.86 respectively).

Table 4: Main results for 'curved', 'sharp' and 'sharper' bending micro-channels.

	$\Omega_{channel,5}$ '*curved*'	$\Omega_{channel,5}$ '*sharp*'	$\Omega_{channel,5}$ '*sharper*'
Migration behaviour	Permeative	Permeative	Permeative
Covered distance (μm)	46.3	45	39.7
Average migration velocity (μm/s)	$1.4 \cdot 10^{-2}$ max $2.4 \cdot 10^{-2}$	$0.8 \cdot 10^{-2}$ max $1.4 \cdot 10^{-2}$	$0.9 \cdot 10^{-2}$ max $2.3 \cdot 10^{-2}$
Entry time $t_{contact}$(s)	2700	2700	2700
Exit time t_{exit} (s)	7800	-	-
Penetration period T_{entry}(s)	5100	-	-
Maximal cell area/nucleus area (during T_{entry})	3.6	3.63	3.65
Minimal cell area/nucleus area (during T_{entry})	2.6	2.86	2.73
Maximal frontal cell-substrate surface force before $t_{contact}$ and after t_{exit} [Pa]	9.5	9.5	9.5
Maximal rear cell-substrate surface force before $t_{contact}$ and after t_{exit} [Pa]	2.8	2.8	2.8
Frontal cell-substrate surface force at $t_{contact}$ [Pa]	7.5	7.5	7.5
Rear cell-substrate surface force at $t_{contact}$ [Pa]	-	-	-
Cell-channel surface force at $t_{contact}$ [Pa]	1	1	1
Maximal cell-channel surface force during T_{entry} [Pa]	4.5	8.5	14.5

It is possible to notice that for the 'curved' bending (Fig. 6a), the cell comes into contact only with the upper wall of the micro-channel, while for the 'sharp' and 'sharper' bending (Fig. 6b,c respectively) the contact occurs with both the upper and the lower walls. The contact time $t_{contact}$ is the same for the three configurations and equal to 2700 s. However, the exit time t_{exit} has been determined only for the 'curved' bending (7800 s), while for the other two cases the cell does not loose contact with the micro-channel walls during the simulation interval.

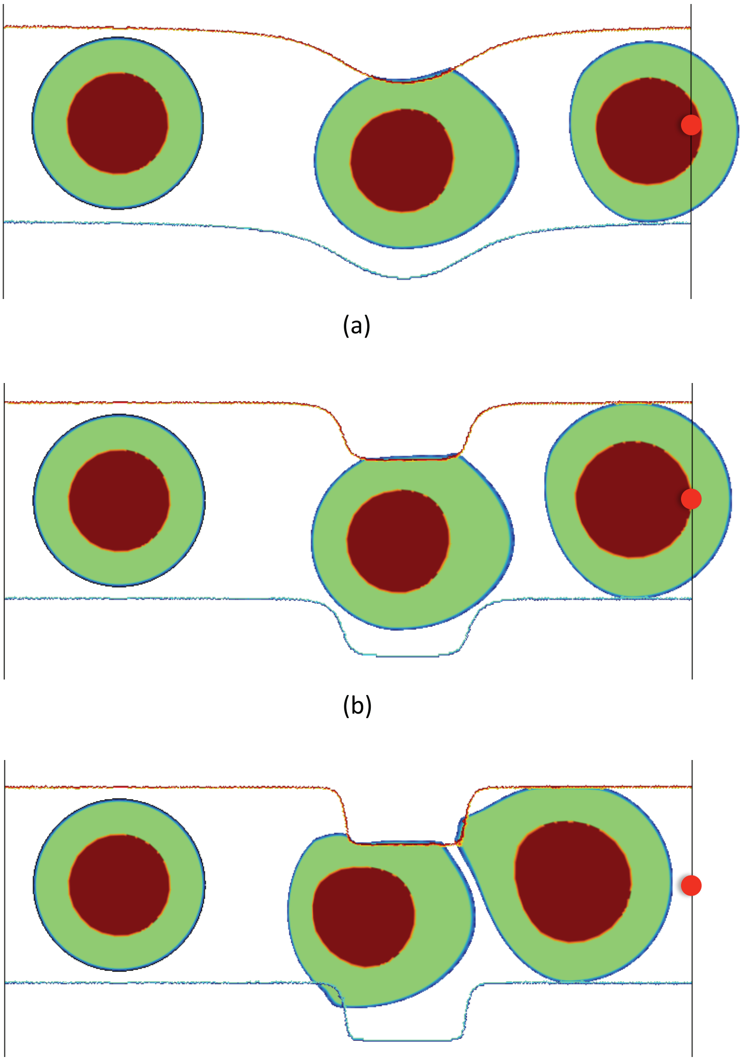

(a)

(b)

(c)

Figure 6: Migration through bending micro-channels (a) ‘Curved’ micro-channel (from left to right t = 0, 5000 s, 9000 s) (b) ‘Sharp’ micro-channel (from left to right t = 0, 5000 s, 9000 s) (c) ‘Sharper’ micro-channel (from left to right t = 0, 5000 s, 9000 s) (blue= cell cortex, green = cytosol, orange = nuclear lamina, red = nucleoplasm, red circle = attractive source).

Regarding the surface forces, the values found are very close to those of previous micro-channels especially for the maximal frontal (9.5 Pa) and rear (2.8 Pa) cell-substrate force before $t_{contact}$ and after t_{exit}. At $t_{contact}$, only the frontal cell-substrate force has been evaluated and is equal to 7.5 Pa and the cell-channel force is equal to 1Pa for the three configurations. Finally, the maximal cell-channel force during T_{entry} increases as the entry angle becomes sharper and is equal to 4.5 Pa, 8.5 Pa and 14.5 Pa respectively for the 'curved', 'sharp' and 'sharper' bending.

3.3 Critical role of mechanics

The current model represents an extension of the work proposed in [23]. In fact, the same mechanical principles are employed, but the characteristic functions used to define the micro-channels allow obtaining more complex geometries combining constriction and curved rigid walls, which induce the cell to turn or squeeze or both simultaneously in order to be permeative.

Let us compare the present results to those found in [30] and [23]. In [30], the cell migrates over a 2D flat substrate with slippery regions on it which inhibit the efficient migration. In that model, an external attractive source is introduced and the cell is equipped either with a distance or a velocity sensor, which allows detecting the slippery regions. Then, the cell is able to turn left or right and to completely or partially avoid the 'obstacles' in order to get to the source as fastest as possible. In some sense, the cell possesses an intrinsic will thanks to which it is able to adapt itself to the external environment. In [23], the cell migrates along the horizontal axis $\boldsymbol{i}_x$ across micro-channels of different widths leading to straight constrictions from sub-cellular to sub-nuclear dimensions. In this case, without any inherent or *a priori* decision, the cell adjusts its movement and shape according to the surroundings and its behaviour (permeative, invasive or penetrating) highly depends on the nucleus ability to deform.

The present model includes two main aspects from the previous works, but some differences can be pointed out. First, due to the curved rigid walls of the micro-channels, the cell must turn left or right to achieve the opposite side, but no intrinsic decision is considered. However, such behaviour is rather determined by the surrounding mechanical environment. A significant example is provided by $\Omega_{channel,4}$. In this configuration in fact, the cell turns right to avoid the central obstacle, but such a choice is not determined by a *a priori* decision (as it was the case in [30]), but probably triggered by some viscoelasticity effects. Second, the cell has to squeeze in order to pass through the micro-channel constrictions, but the narrowing may not be aligned with the direction of migration anymore ($\Omega_{channel,3}$ and $\Omega_{channel,4}$ for instance). Therefore, according to the results, it seems that, by introducing an external attractive source only (Sec. 2.3) and without any intrinsic will, the cell is still able to adapt itself to the micro-channel shape and to migrate across it. These findings demonstrate that mechanics of both the cell and the environment plays a critical role in confined migration and may, alone, provide important insights for the understanding of this phenomenon.

4 Conclusion

The work presented in this paper represents an extension of the previous model proposed in [23]. In fact, a 2D model of a HeLa cell migrating through a micro-channel is still presented. Nonetheless, five new micro-channels are tested combining a curved shape and a constriction. Additionally, for micro-channel $\Omega_{channel,1}$ to $\Omega_{channel,4}$, both sub-cellular (12μm) and sub-nuclear (7μm) constrictions have been obtained, while for $\Omega_{channel,5}$ three types of bending have been investigated (‘curved’, ‘sharp’ and ‘sharper’). For all the configurations, the cell is able to achieve the opposite side of the micro-channel and can therefore be considered as permeative. Several parameters have been evaluated such as the covered distance, the migration velocity, the ratio between the cell area and the nucleus area as well as the cell-substrate and the cell-channel surface forces. The results confirm the fundamental role of mechanical forces during confined migration since, without any additional chemical or molecular input but the external attractive source, the cell is able to adjust its movement and shape to the complex geometry of the environment and migrate through the constricted-curved micro-channels.

References

1. Nourshargh, S., Hordijk, P. L. & Sixt, M. (2010) Breaching multiple barriers: leukocyte motility through venular walls and the interstitium. *Nat Rev Mol Cell Biol*, 11, 366–378.

2. Friedl, P. & Wolf, K. (2010) Plasticity of cell migration: a multiscale tuning model. *J Cell Biol*, 188:11–19.

3. Su, J., Jiang, X., Welsch, R., Whitesides, G. M. & So, P. T. C (2007) Geometric confinement influences cellular mechanical properties I – adhesion area dependence. *Mol Cell Biomech*, 4, 87–104.

4. Richardson WJ, van der Voort DD, Wilson E, Moore JE (2013) Differential orientation of 10T1/2 mesenchymal cells on non-uniform stretch environments. *Mol Cell Biomech*, 10, 245–265.

5. Brock, A. L. & Ingber, D. E. (2005) Control of the direction of lamellipodia extension through changes in the balance between Rac and Rho activities.

Mol Cell Biomech, 2, 135–143.

6. Zaman, M. H., Kamm, R. D., Matsudaira, P. & Lauffenburger, D. A. (2005) Computational model for cell migration in three-dimensional matrices. *Biophys J*, 89, 1389–1397.

7. Zaman, M. H., Matsudaira, P. & Lauffenburger, D. A. (2007) Understanding effects of matrix protease and matrix organization on directional persistence and translational speed in three-dimensional cell migration. *Ann Biomed Eng*, 35, 91–100.

8. Erler, J. T. & Weaver, V. M. (2009) Three-dimensional context regulation of metastasis. *Clin Exp Metastasis*, 26, 35–49.

9. Wolf, K. et al. (2009) Collagen-based cell migration models in vitro and in vivo. *Semin Cell Dev Biol*, 20, 931–941.

10. Provenzano, P. P. et al. (2008) Collagen density promotes mammary tumor initiation and progression. *BMC Medicine*, 6, 11.

11. Egeblad, M., Rasch, M. G. & Weaver, V. M. (2010) Dynamic interplay between the collagen scaffold and tumor evolution. *Curr Opin Cell Biol*, 22, 697–706.

12. Ilina, O., Bakker, G-J., Vasaturo, A., Hofmann, R. M. & Friedl, P. (2011) Two-photon laser-generated microtracks in 3D collagen lattices: principles of MMP-dependent and -independent collective cancer cell invasion. *Phys Biol*, 8, 015010.

13. Heuzé, M. L., Collin, O., Terriac, E., Lennon-Duménil, A-M. & Piel, M. (2011) Cell migration in confinement: a micro-channel-based assay. *Methods Mol Biol*, 769, 415–434.

14. Irimia, D. & Toner, M. (2009) Spontaneous migration of cancer cells under conditions of mechanical confinement. *Integr Biol (Camb)*, 1, 506–512.

15. Rolli, C. G., Seufferlein, T., Kemkemer, R. & Spatz, J. P. (2010) Impact of Tumor Cell Cytoskeleton Organization on Invasiveness and Migration: A Microchannel-Based Approach. *PLoS ONE*, 5, e8726.

16. Faure-André, G. et al. (2008) Regulation of dendritic cell migration by CD74, the MHC class II-associated invariant chain. *Science*, 322, 1705–1710.

17. Taylor, A. M. et al. (2005) A microfluidic culture platform for CNS axonal injury, regeneration and transport. *Nat Methods*, 2, 599–605.

18. Scianna, M., Preziosi, L. (2013) Modeling the influence of nucleus elasticity on cell invasion in fiber networks and microchannels. *J Theor Biol*, 317, 394–406.

19. Scianna, M., Preziosi, L. & Wolf, K. (2013) A Cellular Potts Model simulating cell migration on and in matrix environments. *Math Biosci Eng*, 10, 235–261.

20. Tozluoğlu, M. et al. (2013) Matrix geometry determines optimal cancer cell migration strategy and modulates response to interventions. *Nat Cell Biol*, 15, 751–762.

21. Giverso, C., Grillo, A. & Preziosi, L. Influence of nucleus deformability on cell entry into cylindrical structures. *Biomech Model Mechanobiol*:1–22.

22. Mousavi, S. J., Doweidar, M. H. & Doblaré, M. (2013) Cell migration and cell-cell interaction in the presence of mechano-chemo-thermotaxis. *Mol Cell Biomech*, 10, 1–25.

23. Aubry, D., Thiam, H., Piel, M. & Allena, R. (2014) A computational mechanics approach to assess the link between cell morphology and forces during confined migration. *Biomech Model Mechanobiol*.

24. Scianna, M. & Preziosi, L. (2014) A cellular Potts model for the MMP-dependent and -independent cancer cell migration in matrix microtracks of different dimensions. *Comput Mech*, 53, 485–497.

25. Larson, R. G. (1998) *The Structure and Rheology of Complex Fluids* (Oxford University Press, USA).

26. Holzapfel, G. A. (2000) *Nonlinear Solid Mechanics: A Continuum Approach for Engineering* (Wiley). 1st Ed.

27. Taber, L. A. (2004) *Nonlinear Theory of Elasticity: Applications in Biomechanics* (World Scientific Pub Co Inc).

28. Phillipson, M. et al. (2006) Intraluminal crawling of neutrophils to emigration sites: a molecularly distinct process from adhesion in the recruitment cascade. *J Exp Med*, 203, 2569–2575.

29. Sakamoto, Y., Prudhomme, S. & Zaman, M. H. (2011) Viscoelastic gel-strip model for the simulation of migrating cells. *Ann Biomed Eng*, 39, 2735–2749.

30. Allena, R. & Aubry, D. (2012) “Run-and-tumble” or “look-and-run”? A mechanical model to explore the behavior of a migrating amoeboid cell. *J Theor Biol*, 306, 15–31.

31. Allena, R. (2013) Cell migration with multiple pseudopodia: temporal and spatial sensing models. *Bull Math Biol*, 75, 288–316.

32. Schaub, S., Bohnet, S., Laurent, V. M., Meister, J-J. & Verkhovsky, A. B. (2007) Comparative Maps of Motion and Assembly of Filamentous Actin and Myosin II in Migrating Cells. *Mol Biol Cell*, 18, 3723–3732.

33. Friedl, P., Wolf, K. & Lammerding, J. (2011) Nuclear mechanics during cell migration. *Curr Opin Cell Biol*, 23, 55–64.

34. Ronot, X., Doisy, A. & Tracqui, P. (2000) Quantitative study of dynamic behavior of cell monolayers during in vitro wound healing by optical flow analysis. *Cytometry*, 41, 19–30.

35. Ngalim, S. H. et al. (2013) Creating adhesive and soluble gradients for imaging cell migration with fluorescence microscopy. *J Vis Exp*.

36. Pesen, D. & Hoh, J. H. (2005) Micromechanical Architecture of the Endothelial Cell Cortex. *Biophys J*, 88, 670–679.

37. Tinevez, J-Y. et al. (2009) Role of cortical tension in bleb growth. *PNAS*:pnas.0903353106.

38. Jiang, H. & Sun, S. X. (2013) Cellular Pressure and Volume Regulation and Implications for Cell Mechanics. *Biophysical Journal*, 105, 609–619.

39. Righolt, C. H. et al. (2010) Molecular Image Analysis: Quantitative Description and Classification of the Nuclear Lamina in Human Mesenchymal Stem Cells. *International Journal of Molecular Imaging* 2011. Available at: http://www.hindawi.com/journals/ijmi/2011/723283/abs/ [Accessed September 4, 2013].

40. Crick, F. H. C. & Hughes, A. F. W. (1950) The physical properties of cytoplasm. *Experimental Cell Research*, 1, 37–80.

41. Caille, N., Thoumine, O., Tardy, Y. & Meister, J-J. (2002) Contribution of the nucleus to the mechanical properties of endothelial cells. *J Biomech*, 35, 177–187.

42. Dahl, K. N., Ribeiro, A. J. S. & Lammerding, J. (2008) Nuclear Shape, Mechanics, and Mechanotransduction. *Circulation Research*, 102, 1307–1318.

43. Vaziri, A., Lee, H. & Mofrad, M. R. K. (2006) Deformation of the cell nucleus under indentation: Mechanics and mechanisms. *Journal of Materials Research*, 21, 2126–2135.

44. Christensen, R. M. (1991) *Mechanics of Composite Materials* (Krieger Publishing Company).

45. Bausch, A. R., Möller, W. & Sackmann, E. (1999) Measurement of local viscoelasticity and forces in living cells by magnetic tweezers. *Biophys J*, 76, 573–579.

46. Drury, J. L. & Dembo, M. (2001) Aspiration of human neutrophils: effects of shear thinning and cortical dissipation. *Biophys J*, 81, 3166–3177.

47. Fukui, Y., Uyeda, T. Q. P., Kitayama, C. & Inoué, S. (2000) How well can an amoeba climb? *PNAS*, 97, 10020–10025.